PCCP

Accepted Manuscript

ROYAL SOCIETY OF CHEMISTRY

www.rsc.org/pccp

Journal Name

RSCPublishing

ARTICLE

Cite this: DOI: 10.1039/x0xx00000x

Received 00th January 2012,
Accepted 00th January 2012

DOI: 10.1039/x0xx00000x

www.rsc.org/

Tunable Thermal Conductivity of Thin Films of Polycrystalline AlN by Structural Inhomogeneity and Interfacial Oxidation

J. Jaramillo-Fernandez [a], J. Ordonez-Miranda [b], E. Ollier [a] and S. Volz [b*]

The effect of the structural inhomogeneity and oxygen defects on the thermal conductivity of polycrystalline Aluminum Nitride (AlN) thin films deposited on single-crystal silicon substrates is experimentally and theoretically investigated. The influence of the evolution of crystal structure, grain size, and out-of plane disorientation along the cross plane of the films on their thermal conductivity is analyzed. The impact of oxygen-related defects on thermal conduction is studied in AlN/AlN multilayered samples. Microstructure, texture, and grain size of the films were characterized by X-ray diffraction and scanning and transmission electron microscopy. The measured thermal conductivity obtained with the 3-omega technique for a single and multiple layers of AlN are in fairly good agreement with the theoretical predictions of our model, which is developed by considering a serial assembly of grain distributions. An effective thermal conductivity of 5.92 $Wm^{-1}K^{-1}$ is measured for a 1107.5 nm-thick multilayer structure, which represents a reduction of 20% of the thermal conductivity of an AlN monolayer with approximately the same thickness, due to oxygen impurities at the interface of AlN layers. Our results show that the reduction of the thermal conductivity as the film thickness is scaled down is strongly determined by the structural inhomogeneities inside the sputtered films. The origin of this non-homogeneity and the effect on phonon scattering are also discussed.

Keywords: Polycrystalline thin films; Grain geometry; AlN; Thermal conductivity.
PACS: 65.40.-b; 81.07.Bc; 81.15.Aa; 81.15.Cd

1 Introduction

Thermal conductivity of polycrystalline thin films is of fundamental importance for a large number of applications, ranging from thermoelectric devices for energy conversion to heat dissipation in thermal management[1,2]. Unlike their single-crystal bulk counterparts, nanocrystalline materials generally exhibit an anisotropic and heterogeneous structure which is composed of grains with irregular shapes and sizes[3,4]. In addition to the complex grained structure in polycrystalline thin films, various crystallographic defects, such as dislocations, vacancies, interstitial voids, mass differences, and substitutional impurities are usually present[5]. Interactions of the heat carriers with these point-like and planar defects increase the scattering events that significantly reduce the thermal conductivity from that of the corresponding single-crystal counterpart[6–8]. These changes in the transport properties are particularly important when the size of the grains in nanoscale structured materials is comparable to the mean free path of the heat carriers[9]. Conduction of heat in perfect single-crystalline thin films has been widely studied in the literature, both theoretically[10–19] and experimentally[20–25]. Nevertheless, in spite of its importance in new technological applications, the accurate description of the thermal properties of polycrystalline thin films has been much less explored and it remains a challenging task, because of the complexity of the structure of these materials and the large number of scattering mechanisms implied. Braginsky et al.[24] proposed a phonon-hopping formalism, based on the assumption of scattering at the grain boundaries as the main mechanism limiting thermal conductivity of granular materials. Yang et al.[25] observed experimentally a strong grain size effect on the thermal conductivity of nanocrystalline yttria-stabilized cubic zirconia films, over a range of 10 to 100nm. In order to provide more accurate predictions for nanograined materials, MonteCarlo (MC) simulations[26] and numerical solutions of the Boltzmann transport equation (BTE)[27–29] were implemented, considering the structure geometry and interface thermal resistance (Kapitza resistance). More recently, Hao[32,33] developed a modified effective medium formulation considering the frequency dependence of phonon properties to obtain the lattice thermal conductivity of general nanograined polycrystals. A comparison of the results obtained in these two latter works agreed well with MC simulations for silicon[34] and lead telluride[35] polycrystals at 300 K, both in the frequency-dependent[34] and the frequency-independent[36] cases. Yet, these theoretical formalisms have not been applied and compared to experimental observations. To describe thermal properties of polycrystals, the previous works considered either a distribution function of grains of a given size[37] or an effective grain size[32]. However, the size and morphology of the grains as well as the orientation of crystallites in "real" polycrystalline thin films are typically non-uniform and evolve along the axis normal to the film surface[4,38–41], causing a structural non-homogeneity. In the reported literature, the role of the structural inhomogeneity along the film thickness in thermal properties has not been experimentally studied neither described theoretically. This is mainly due to the fact that the accurate predictions and experimental characterization of the polycrystalline thin film structure evolution are quite difficult.

Thermal properties of polycrystalline Aluminum Nitride (AlN) thin films are crucial for many engineering applications, including surface acoustic wave (SAW) devices, light emitting diodes (LED), high electron mobility transistors (HEMTs), heat sinks in micro-electronic packaging, and dielectrics films in thermal management. Additionally, AlN thin films exhibit the mentioned characteristic structural non-homogeneity, like other materials of great technological interest, such as GaN, diamond or ZnO. Recent works have reported values for the effective thermal conductivity of polycrystalline AlN thin films at room temperature on different substrates in the range of 0.5-50 $Wm^{-1} K^{-1}$ [42–47]. Thickness dependence of the thermal conductivity is somehow addressed in these works, as well as other factors that significantly affect the thermal transport such as synthesis conditions, microstructure, grain size, and substrate surface roughness, which are evoked. However, the correlation between thermal conductivity and both the morphology and the grain structure evolution along the cross-plane direction of AlN thin films has not been systematically investigated yet. Research on the physical description of scattering phenomena at the interface, grain boundaries, and oxygen related defects, as a function of the characteristic structural heterogeneity in polycrystalline thin films, is therefore required.

In this work, the thermal transport across polycrystalline AlN sputtered films deposited over a silicon substrate is experimentally and theoretically investigated. We analyze the impact of oxygen related defects in thermal conduction and the effects of the size, shape, and morphology evolution of grains along the axis normal to the film surface on the phonon thermal transport properties. Microstructure, texture, crystallite size and interfacial atomic structure of the films are characterized experimentally. 3-omega measurements as a function of film thickness were carried out to correlate structural features with thermal conductivity. Moreover, by considering the grains like a serial assembly of right parallelepipeds, we develop a theoretical model for the thermal conductivity of AlN thin films, and show that their predictions are in fairly good agreement with our experimental data.

The theoretical and experimental results presented in this work are expected to be useful in the description and understanding of thermal transport in nano and microscale polycrystalline thin films that exhibit the mentioned characteristic structural non-homogeneity. As these materials are of great importance in new technological applications, our results may be helpful to understand the thermal performance of electronic devices and thermoelectric materials.

2 Experimental procedure

To understand and isolate the effects of morphology and atomic structure on thermal properties, we studied the thermal conductivity of monolayer and multilayer aluminum nitride thin films as a function of film thickness.

2.1 Film Deposition by Sputtering

Different samples with thickness varying from 270 nm up to 1500 nm were prepared by reactive radio-frequency (RF) magnetron sputtering on single-crystal Si (100) substrates in a high vacuum chamber with a base pressure of $4x10^{-8}$ mbar. Samples were sputtered without any external heating from a pure metallic aluminum target of 8-inch diameter in a high purity mixture (99.99%) of nitrogen (N_2) and argon (Ar). To allow cleaning of the target surface and plasma stabilization, the target was pre-sputtered for 30 minutes in pure Ar, prior to film deposition.

In order to promote better conditions for AlN nucleation on the surface of silicon substrate, we operated a two-step deposition process[48,49]. In the first stage, additional energy was supplied to the adatoms by increasing the RF target power and by decreasing the deposition pressure, in order to increase the surface energy to the substrate and enhance the mobility of impinging species. This additional energy supply was carried out at the expense of uncontrolled residual stress. Moreover, the first step was performed with a higher nitrogen content in order to operate in a deeper poisoned mode and promote the nucleation of small c-axis oriented grains[49]. This base layer, which acts as a seed layer, promotes the orientation of the subsequent film growth. During the second stage, deposition was performed at higher pressure and moderate RF target power, to reduce the residual stress and favor well aligned columnar growth. Deposition parameters for preparing the AlN films are summarized in Table 1. The deposition time varied from 30 to 164.5 minutes, depending on the film thickness.

Table 1. Fixed deposition parameters for AlN thin films.

Substrate	Si (100)	
Substrate temperature (K)	≈ 300	
Target	Al (99.99% purity)	
Gas	Ar, N2	
Base pressure (10-8mbar)	4	
	Step 1	Step 2
Sputtering pressure (10-3mbar)	1.5	2
Ar flow rate (sccm)	198	194
N2 flow rate (sccm)	8	2
RF Power (W)	500	400
Deposition time (minutes)	2	30 -164.5

AlN/AlN multilayer samples were prepared to understand the role of nanoscale defects induced by oxygen impurities on thermal transport properties of polycrystalline thin films. Multilayer preparation aimed at introducing random oxygen impurities at the interface between two AlN layers, deposited one on the top of the other. The experimental process consisted of two iterative steps: First, an AlN layer of 270 nm thick was deposited under the sputtering conditions presented previously. After film deposition, the process was interrupted by stopping the pumping system and venting the deposition chamber to atmospheric pressure. The iterative interruption of the sputtering process enabled the preparation of multilayer samples, which consisted of two, three, and four AlN layers of 270 nm thick, deposited one on the top of the other.

Film thicknesses and microstructures were characterized by field-emission gun scanning electron microscopy (ZEISS LEO 1530). Texture evolution along the cross-plane, atomic structure, grain boundaries, and crystallite sizes were studied by transmission electron microscopy (FEI Tecnai Osiris 200kV TEM). Grain size distributions were obtained by statistical analysis from digitally processed images and the chemical analysis was performed by energy-dispersive X-ray spectroscopy (EDX). Furthermore, preferred orientation, crystalline structure, and out-of-plane disorientation were characterized by θ-2θ and ω X-ray diffraction (XRD) patterns, respectively.

2.2 Thermal Conductivity Measurement by the 3ω Method

Thickness-dependent thermal conductivity measurements were performed by the 3ω method, inducing harmonic Joule heating in a gold-titanium strip deposited by pulsed DC sputtering on AlN films. The micro-fabricated metal strip served as a heater and temperature-measuring probe due to its temperature dependent electrical resistance. The nominal length, width, and thickness of the patterned Au strip were 4000 µm, 10 µm, and 250 nm respectively, including a 20 nm thick Ti layer that improved adhesion. To measure the cross-plane thermal conductivity, an alternating electrical current with angular modulation frequency $\omega = 2\pi f$ was applied through the metal strip inducing a temperature oscillation at a doubled frequency 2ω, whose amplitude depends on the underlying matter. The fundamental modulation frequency ω was varied from 10 Hz to 1 kHz. The use of an alternating current and the reduced characteristic length of the experimental geometry allowed to analyze a very small volume of the sample and to be weakly sensitive to heat lost by convection and radiation due to the confinement of the heat wave inside the sample and to the rapid decay of the themperature oscillations compared to the characteristic radiative times[50].

Considering the typical values of the heat capacity ($c_p = 711\,\mathrm{J/kg\cdot K}$), the density ($\rho = 2330\,\mathrm{kg/m^3}$) and the thermal conductivity ($k_{si} = 147\,\mathrm{W/m\cdot K}$) of silicon[51], and taking into account that the thermal oscillation propagates into the specimen with a penetration depth δ_{tw} [52] that is proportional to the square root of the modulation frequency,

$$\delta_{tw} = \sqrt{\frac{k_{Si}}{2\omega\rho C_p}}\,, \tag{1}$$

we estimated that the thermal wave travels a distance from 84 µm up to 840.3 µm inside the prepared samples. Since these penetration depths are larger than the film thicknesses in all the evaluated frequency range, the contribution of the native oxide layer formed at the surface of the silicon substrate, which was evidenced by EDX analysis (Fig. 11), has to be necessarily taken into consideration. This oxide layer usually shows up in experiments conducted in ambient air[53,54], as is our case.

To measure the cross-plane thermal conductivity of the AlN films, the voltage drop across the metal strip, which depends on the temperature rise caused by the underlying matter, was measured by a signal processing lock-in amplifier. Yet, the obtained overall temperature rise was generated by the AlN film and the native silicon oxide layer. To isolate the signal drop exclusively caused by the AlN film, a differential 3-omega method was applied. In the differential approach, the thermal conductivity is obtained by measuring two similar structures, one with the AlN film, the other one without the studied film, serving as the reference sample. Hence, the average temperature rise difference was obtained by removing the signal of the reference sample from that of the specimen with the deposited AlN layer, to isolate the thermal properties of the film. The native oxide contribution was therefore subtracted from the total experiment temperature rise [Eq. (2)], which was obtained at comparable power inputs by similar heaters deposited on the AlN film and a reference Si/SiO$_2$ structure without the studied film. Under this condition, the effective thermal conductivity of the film is given by[53]

$$k_{eff} = \frac{L}{2}\left[\left(\frac{2V_{3w}\,b}{P_l\,\alpha\,V_{1w}}\right)_{R+F} - \left(\frac{2V_{3w}\,b}{P_l\,\alpha\,V_{1w}}\right)_{R}\right]^{-1}_{average}, \tag{2}$$

L being the thickness of the film, $2b$ the width of the strip, P_l the power per unit of length in the strip and α the temperature coefficient of electrical resistance. The subscripts $R+F$ and R correspond to the AlN sample and the reference structure without the AlN film, respectively.

Given that in our experiments, the thermal conductivity of the silicon substrate is at least 20 times higher than the one of the AlN films and the heater width is 10 times larger than the film thickness, a one-dimensional heat conduction model was used to fit the real part of the temperature oscillation amplitude as a function of heating frequency [53].

To obtain the thermal boundary resistance R_s between the AlN layer and the substrate, the whole system was considered as a thermal resistance network, such that

$$\frac{L}{k_{eff}} = \frac{L}{k_{AlN}} + R_s\,. \tag{3}$$

Assuming that R_s is equivalent for all samples, R_s is determined by fitting Eq. (3) to the experimental data of the thermal resistance L/k_{eff} against the layer thickness L, and extrapoling the linear model to $L=0$. For the multilayer AlN films, an additional thermal boundary R resistance at interfaces between two AlN layers has to be considered and Eq. (3) is replaced by

$$R = \frac{R_{eff} - R_s - NR_{AlN}}{N-1}, \qquad (4)$$

N being the number of AlN layers and R_{AlN} the intrinsic thermal resistance of each AlN layer.

The experimental setup of the 3ω technique is shown in Fig.1, and it consists of a low frequency analog sine wave generator Krohn Hite 4402b with a frequency range from 1 Hz to 110 kHz and a harmonic distortion of 0.0005%, a signal conditioning stage used to filter and amplify the signal, a processing stage controlled by a PowerDAQ data acquisition card (UEI PD2-MFS-4-2M/14DG), a computer, and a LABVIEW® software employed to detect the 3ω signal. As the amplitude of the third harmonic voltage is three orders of magnitude smaller than the fundamental component, a signal conditioning stage composed of operational amplifiers was used to subtract the 1ω component of the measured signal.

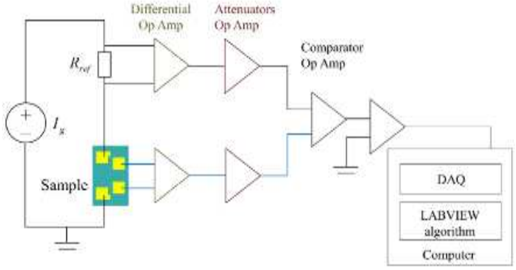

Fig. 1. Scheme of the experimental setup used for the 3ω measurements. The 3-omega experimental setup uses a microfabricated strip as a heater and temperature-measuring probe. An analogue sine wave generator generates a 1ω current, which produce periodic heating in the 3-omega pattern. A digital lock-in amplifier acquires the sample-dependent temperature response through an electronic conditioning stage employed to perform the signal treatment.

The uncertainty on the measured k_{eff} arises from the uncertainties on the strip width, the film thickness, and the temperature coefficient of resistivity measurements. The parameters α, L, and $2b$ were therefore measured separately for every sample. To determinate the temperature coefficient of resistivity α, variations of the electrical resistance as a function of the temperature were measured by the four points probe method. The sample was placed in a vacuum chamber, and a step-wise temperature program was used, holding the sample at constant temperature until thermal equilibrium was reached. α was then determined from the slope of the electrical resistance versus temperature.

3 Thermal conductivity model

To develop a model for the thermal conductivity of polycrystals, taking into account the distribution of the grain shape and size, AlN thin films are modeled as a serial assembly of grains which evolve along the cross-plane. Fig. 2 shows a schematic representation of the distribution of the grain structure along the c-axis established from a transmission electron microscopy analysis of the sputtered AlN thin films[38], which is presented in section 4.1, below. Based on the spatial distribution of grains inside the film samples, each layer can be divided in three sub-layers, namely the near-interface, transition, and columnar regions. Therefore, different grain size distributions and shapes were considered for each region of the film. Cubic grain shapes with average lengths d and c were assumed for the near-interface and transition regions, respectively. For the columnar region, we consider the grains as right parallelepipeds with an average length a for each side of the base and an average height b [Fig. 2(b) and(c)]. As shown in Fig. 2(a), d_i, d_t, and b are the thickness of the near-interface, transition, and columnar regions, respectively.

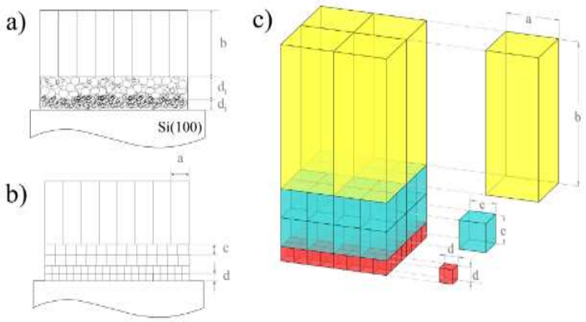

Fig. 2. a) Scheme of the grain structure of the AlN films on Si (100) along the cross-plane, according to ref. [38]. Modeled grain structure in 2d b) and in 3d c), consisting of cubic grain shapes for the near-interface and transition regions, and right parallelepipeds grain shapes for the columnar region.

The effective thermal conductivity k_{eff} of the multilayered films is given by Eq. (4), which in terms of thermal conductivity k_{AlN} of each layer of thickness L, reads

$$\frac{NL}{k_{eff}} = \frac{NL}{k_{AlN}} + (N-1)R + R_s. \qquad (5)$$

Under the *three sub-regions* consideration, a film of AlN behaves as a serial assembly of three layers and therefore its cross-plane thermal conductivity k_{AlN} can be calculated as a sum of thermal resistances in series, as follows

$$\frac{L}{k_{AlN}} = \frac{L_I}{k_I} + \frac{L_T}{k_T} + \frac{L_C}{k_C}, \qquad (6)$$

where k_n stands for the thermal conductivity of the interface $(n=I)$, transition $(n=T)$, and columnar $(n=C)$ regions, L_n are their corresponding thicknesses, and $L = L_I + L_T + L_C$. The values of k_n are given by Majumdar's model,[54]

$$k_n = \frac{k_{0n}}{1 + 4l_n/3L_n}, \qquad (7)$$

where l_n is the mean free path (MFP) of phonons inside the region n and k_{0n} is its thermal conductivity when $L_n \to \infty$. Equation (7) is valid for diffuse scattering of phonons at the boundaries of each region. Given the grained structure of the prepared samples, this type of scattering is expected to be dominant and hence the application of Eq. (7) for modeling the thermal conductivity is well justified. Because of the irregular geometry and the increasing interfacial scattering of phonons as the grain size is scaled down, the determination of k_{0n} and l_n is very difficult. As a first approximation, the grains are going to be represented by right parallelepipeds, as shown in Fig. 2. Under this condition, the grained AlN behaves as a serial assembly of grains and hence its bulk thermal conductivity k_{0n} is given by

$$\frac{d_n}{k_{0n}} = \frac{d_n}{k_{gn}} + R_g, \tag{8}$$

where k_{gn} is the thermal conductivity of a single grain with an average size d_n in the direction of heat conduction in the region n and R_g is the average interface thermal resistance among grains. Taking into account that the intrinsic MFP (l_0) of phonons inside the grains can be of the order of d_n, the dynamics of these energy carriers is not only driven by the interactions among them, but also by their collisions with the inner surface of the grains, as shown in Fig. 3. According to the Matthiessen rule[55], the effective MFP (l_n) of the carriers in each grain (and therefore in each region) is given by

$$\frac{1}{l_n} = \frac{1}{l_0} + \frac{1}{D_n}, \tag{9}$$

where l_0 and D_n are the MFP due to the carrier-carrier and carrier-boundary scattering processes, respectively. These two scattering mechanisms are considered to be independent of each other, and therefore D_n is given by the average distance traveled by phonons inside the grains. The grain thermal conductivity k_{gn} of the grained AlN can then be estimated through the relation $k_{gn} = \rho_n c_n v_n l_n/3$, where ρ_n and c_n are the density and specific heat of AlN, respectively; and v_n is the average phonon speed. Assuming that ρ_n, c_n, and v_n do not change significantly by the presence of grains, the combination of this relation with Eq. (9) yields

$$k_{gn} = \frac{k_0}{1 + l_0/D_n}, \tag{10}$$

where $k_0 = \rho_n c_n v_n l_0/3$ is the bulk thermal conductivity of AlN in absence of grains. By combining Eqs. (8) and (10), it is obtained

$$k_{0n} = \frac{k_0}{1 + l_0/D_n + a_{Kg}/d_n}, \tag{11}$$

where $a_{Kg} = R_g k_0$ is the so-called Kapitza radius of grains. Equation (11) shows that the interface effect becomes stronger for smaller grains, and it appears for grains with a size comparable to or smaller than the grain Kapitza radius ($d_n \le a_{Kg}$). The combination of Eqs. (6), (7) and (11) yields

$$\frac{k_0}{k_{AlN}} = 1 + \frac{l_0}{L}\left(4 + \sum_n \frac{L_n}{D_n}\right) + \frac{a_{Kg}}{L}\sum_n\left(\frac{L_n}{d_n} + \frac{l_0/d_n}{1 + l_0/D_n}\right), \tag{12}$$

where the sums are evaluated for the three regions inside the layers ($n = I, T, C$). Note that the contribution of a_{Kg} to the reduction of the thermal conductivity k_{AlN} is weighted by the total number of grain rows, which is given by $\sum_n L_n/d_n$. For diffusive scattering of phonons at the grain interfaces, the value of R_g (and hence of a_{Kg}) is given by $R_g = 2/(\rho c_p v)_{AlN}$ [13].

By using the typical values for the density ($\rho = 3260$ kg/m^3), specific heat capacity ($c_p = 600$ J/kg·K), and phonon speed ($v = 4210$ m/s) in AlN at room temperature, we obtain $R_g = 2.4x10^{-10}$ m^{2}K/W, which is two orders of magnitude smaller than the thermal resistances of the layer-substrate and layer-layer interfaces, as shown in the section 4.4. This indicates that the grain-grain interface has a relatively small contribution to the reduction of k_{eff}, as established by Eqs. (5) and (12).

To determine D_C, we assume that the energy carriers undergo diffusive scattering at the grain interfaces. This means that the carriers are reflected from the grain interfaces with equal probability to any direction, as is the case of rough interfaces. According to Fig. 3, the symmetry of the problem establishes that the mean distance from an arbitrary point $A = (x, y, 0)$ on the plane $z = 0$ to any other point on the four adjacent planes is the same. In terms of the points $B = (\eta, 0, z)$ and $D = (\xi, w, b)$ on the adjacent and parallel planes to $z = 0$, this condition yields $5D_C = 4I_1 + I_2$, where

$$I_1 = \frac{1}{a^3 b}\int_0^b\int_0^a\int_0^a\int_0^a \sqrt{(x-\eta)^2 + y^2 + z^2}\, dx\, d\eta\, dy\, dz, \tag{13a}$$

$$I_2 = \frac{1}{a^4}\int_0^a\int_0^a\int_0^a\int_0^a \sqrt{(x-\xi)^2 + (y-w)^2 + b^2}\, dx\, d\xi\, dy\, dw. \tag{13b}$$

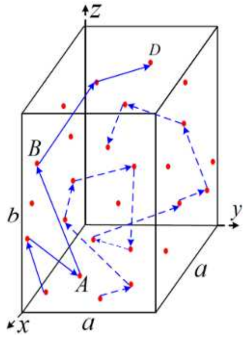

Fig. 3. Carrier-carrier (dashed arrows) and carrier-boundary (solid arrows) scattering processes inside a parallelepiped grain.

The integrals in Eqs. (13a) and (13b) can conveniently be evaluated using a proper computer software, such as Mathematica, Matlab, or Maple. The obtained result for the MFP D_C due to phonon-interface collisions is shown in Fig. 4. Note that for large parallelepiped grains ($b >> a$), D_C exhibits a linear behavior with the size equal to thelengths of the grain.

On the other hand, for cubic grains ($b = a$), $D_C = 0.926a$, which indicates that the mean distance between two random points on different faces of a cube is slightly (7.3%) smaller than the length of its sides. The geometric MFPs inside the cubic grains of the near-interface and transitions regions (Fig. 3) are then given by $D_I = 0.926d$ and $D_T = 0.926c$, respectively.

Finally, Eqs. (10) and (12) establish that the effective thermal conductivity k_{eff} of the multilayer structure is given by

$$k_{eff} = \frac{k_0}{\dfrac{k_0}{k_n} + \dfrac{a_{Ks}}{NL} + (N-1)\dfrac{a_K}{NL}} , \qquad (14)$$

where $a_{Ks} = R_s k_0$ and $a_K = R k_0$ are the Kapitza radii of the substrate-layer and layer-layer interfaces, respectively. The denominator in Eq. (14) represents the reduction of the bulk thermal conductivity k_0 due to the effects of the grain size, layer thickness, and interface thermal resistance.

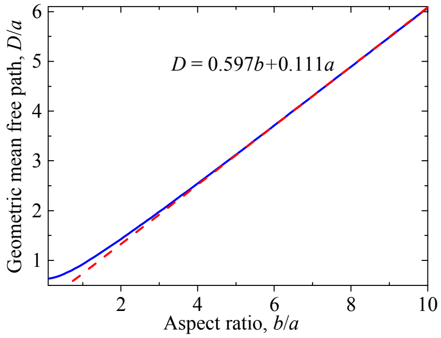

Fig. 4. Mean free path of phonons due to their collisions with the inner surface of a parallelepiped grain.

The contribution of each of these parameters is determined by their relative values with respect to the total thickness of the film. For the monolayer structure (N=1), the effect of a_K disappears, as expected. The bulk thermal conductivity $k_0 = 250\,\mathrm{W/m\cdot K}$ and phonon MFP $l_0 = 110$ nm of AlN are taken from the literature, to determine the theoretical value of k_{eff} with Eq. (14). All the other parameters involved in Eqs. (12) and (14) are measured experimentally, and they are summarized in Table 2, presented in section 4.4 below.

4 Results and discussion

4.1 Microstructure analysis

Figure 5 shows XRD θ-2θ spectra of the monolayer and multilayer AlN samples. Both configurations exhibit strong fiber texture, indicated by the single (002) AlN peak near 2θ = 36.04° which was observed in all samples. The additional peak located at 2θ = 32.91° is associated to the forbidden (200) reflection of Si(100) substrate, which should be absent by symmetry but appears as a result of multiple diffraction effects[58]. The intensity of the (002) AlN diffraction peak increases with the film thickness, for both the monolayer and multilayer systems, as a result of a mixed contribution to coherent scattering of additional atomic planes and higher out-of-plane crystallite alignment [inset in Fig. 5(b)]. The observed (002) peak shift towards higher angles when increasing film thickness is due to strain relaxation mechanisms occurring through the cross-plane[59,60]. This peak shift can be clearly observed by plotting the logarithm of the relative intensity as a function of the 2θ angle, from 34° to 38°, as shown in Fig. S1 of the supplementary material. The increment of the peak intensity as a function of the film thickness measured in multilayers is lower compared to the one in monolayers. The reduced intensity of the diffracted beam is owed to largest crystallite disorientation and to the presence of oxygen-related defects at AlN/AlN interfaces in multilayers, which cause destructive interference of the diffracted X-rays. The average out-of-plane disorientation represented by the full width half maximum (FWHM) of the rocking curve showed in the inset of Fig. 5(b), decreases with the increase of the film thickness. The observed texture sharpening for thicker films results from competitive growth mechanisms that promote overgrowth and coalescence of c-axis oriented grains[4,40]. Moreover, the presence of oxygen atoms at interstitials and lattice sites in AlN multilayers induces planar defects that limit the subsequent well-oriented crystallite growth, therefore increasing the FWHM of the multilayer rocking curves.

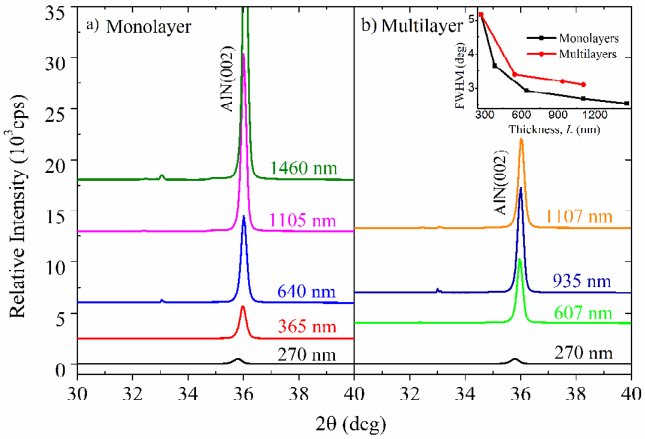

Fig. 5. XRD θ–2θ scan patterns of the AlN a) monolayer and b) multilayer films of different thicknesses. The inset shows (002) XRD rocking curves as a function of the film thickness. The θ-2θ XRD scan of the relative diffracted intensity in logarithmic scale as a function of the 2θ angle, from 34° to 38°, showing the AlN(002) peak shift towards higher angles, can be found in the supplementary material.

The global microstructure of AlN films is showed by the cross sectional bright field TEM image in Fig. 6(a) examined in [0 1 1]Si zone axis orientation. AlN films feature a columnar texture with a clear structural non-homogeneity along the c-axis. Fig. 6(b), 6(c), and 6(d) are atomic resolution micrographs (HRTEM) of different film regions and 6(e), 6(f), 6(g) are the corresponding Fast Fourier Transforms (FFT). Three different structural domains can be identified from Fig. 6(a): the region (1) near the interface with the silicon substrate, which has significant crystallographic disorder and small grains with almost-random crystallographic orientations [Fig. 6(b)]; the microcrystalline transition region (2) between the columnar and near-interface region that features greater grain sizes with a dominant (002) preferred orientation, although other directions are still observed [Fig. 6(c)] and the columnar region (3) where the grains are large with a unique (002) preferred crystalline orientation[38] [Fig. 6(d)]. At the interface with the silicon substrate, a continuous interlayer with a disordered atomic structure is observed within a limited thickness of a few nanometers. Previous works[38,58] have reported that such amorphous interfacial layer is composed of SiO_x and arises either from the native oxide formed at the surface of silicon substrate, or from the reaction of residual oxygen in the vacuum chamber. Other studies attributed the composition of this disordered structure to Si-N bounds creation at the early stage of AlN growth, when N_2 first interacts with the Si substrate[59]. The associated FFT showed in inset of Fig. 6(b) confirms the highly disordered atomic structure of this interfacial layer.

Immediately after the silicon substrate, at the near-interface region [Fig. 6(b)], small crystallites with a near-random orientation distribution are formed. (002) and (100) atomic planes are observed at the early growth stage. However, as revealed by the corresponding heterogeneous FFT spot pattern in Fig. 6(e), these families of planes have different orientations. In the microcrystalline transition region [Fig. 6(c)] between the columnar and the near-interface regions, the observed dominant c-axis preferred orientation is certainly caused by the overgrowth of (002) oriented grains with higher perpendicular growth rate, with respect to other detected orientations [Fig. 6 (f)] [60].The columnar region showed in Fig. 6(d) reveals a highly ordered structure. No in-plane alignment can be inferred from the HRTEM micrograph of two neighbor columns, indicating that AlN films are polycrystalline. Weaker contrast at the grain boundary indicates the presence of local disorder. FFT in Fig. 6(g) scatters the characteristic spots of (002) atomic planes and their (004) reflection, indicating the exclusive presence of the (002) preferred orientation, and thus confirming the high periodicity array of the AlN crystal lattice in the columnar region. The scattered spots have zone axes along the $[11\bar{2}0]$ and $[10\bar{1}0]$ directions.

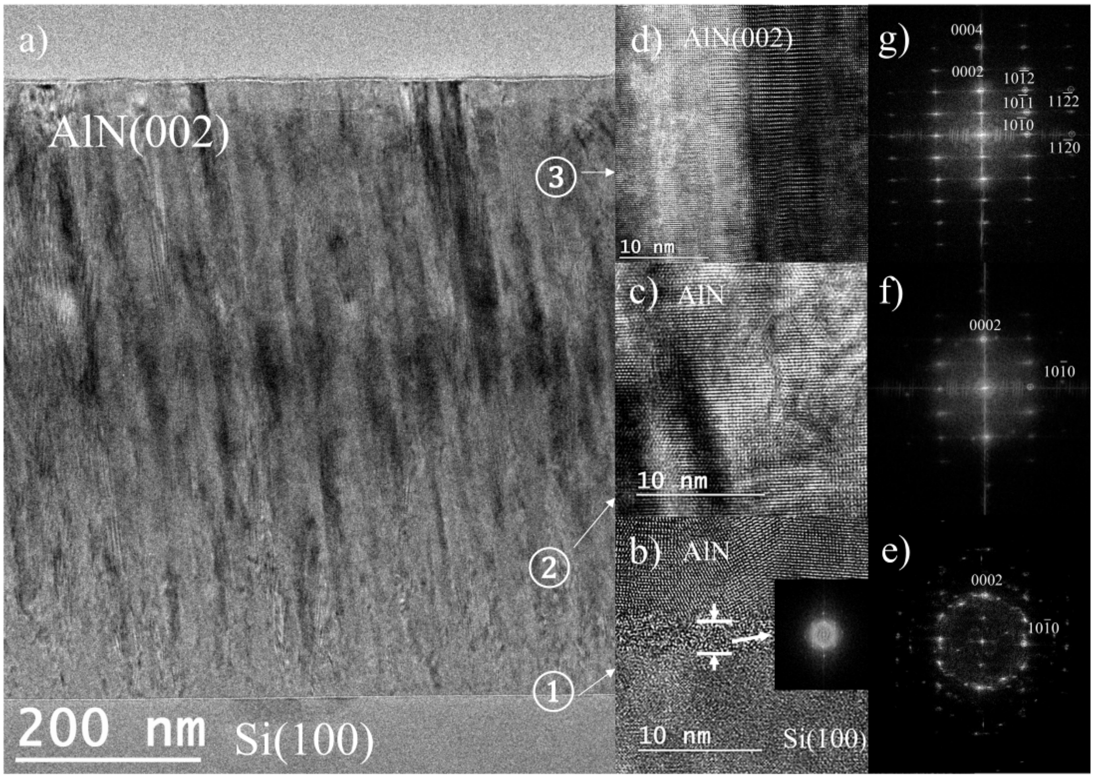

Fig. 6. a) Cross sectional bright field TEM image of a highly c-axis oriented 640nm thick AlN film, obtained along the zone axis of [0 1 1]Si. HRTEM closer-up view of b) the near-interface region, revealing an amorphous-like layer of ≈ 3 nm at the Si/AlN interface, c) the microcrystalline transition region, and d) the columnar region, with their corresponding indexed FFTs e), f) et g) respectively. The inset in b) shows the characteristic FFT pattern of an amorphous continuous interlayer. The indexed FFT pattern of the silicon substrate can be found in the supplementary material.

4.2 Grain Size Distributions

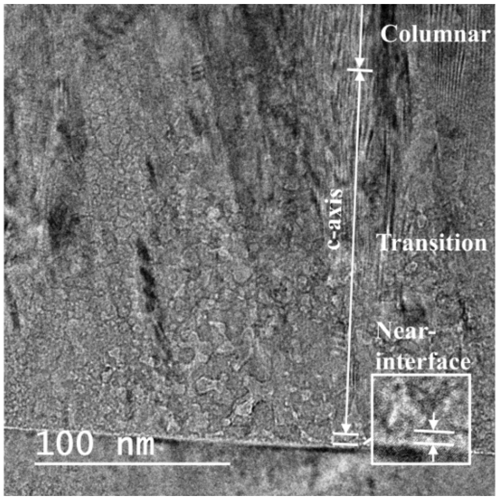

Fig. 7. Evolution of the grained structure through the c-axis from small grains at the near-interface region to aligned grains in the columnar region. The inset shows a closer-up view of the near-interface region.

The microstructure of the interface and transition zones is shown in Fig. 7. AlN films are made of small grains of different sizes and shapes in the region near the silicon substrate. To accurately determine the thermal conductivity of such complex-grained structure, it is necessary to experimentally characterize the evolution of grains, considering the different crystallite size distributions and shapes along the cross plane.

Digital image processing to measure the grain size distributions from scanning transmission microscopy images is not straightforward. The ordered arrays detected by the transmission electron microscope generate a noisy background with frequency components which are different from the grain frequencies. A spiral phase digital filter was hence applied to enhance the crystallite edge detection. The filter assigns a phase or field discontinuity to each structure and thus convolves the obtained pattern to a function of the form $exp[i \tan(f_y/f_x)]$, where f_x and f_y are the frequency coordinates from the image. The results obtained by the implementation of the spiral phase filter are shown in Fig. 8(a). After filter application, human intervention was still needed to refine crystallite identification to carry out the grain size distribution measurements. The *analyze particles* module of *imagej*® software was used to identify, count, and measure the total area of each crystallite. Fig. 8(b) shows the measured grains used to estimate the grain size distributions for an 850 nm-thick monolayer sample. The crystallite size distribution for the near-interface and transition regions were determined, considering the grains like cubes with average lengths d and c for the near-interface and transition regions, respectively [Fig. 2(b) and (c)]. Figure 9 shows the grain size distributions in both the interface and transition regions of 640 nm and 850nm-thick samples obtained by digital image processing. The mean size was calculated by using the distribution function $y(x)$, as follows

$$\overline{x} = \frac{\int_{x_{\min}}^{x_{\max}} x\, y(x)dx}{\int_{x_{\min}}^{x_{\max}} y(x)dx} \tag{15}$$

Were $\overline{x}$ is the average grain size, x is the grain size, and $x_{\min}$ and $x_{\max}$ are the smallest and the biggest grain size, respectively.

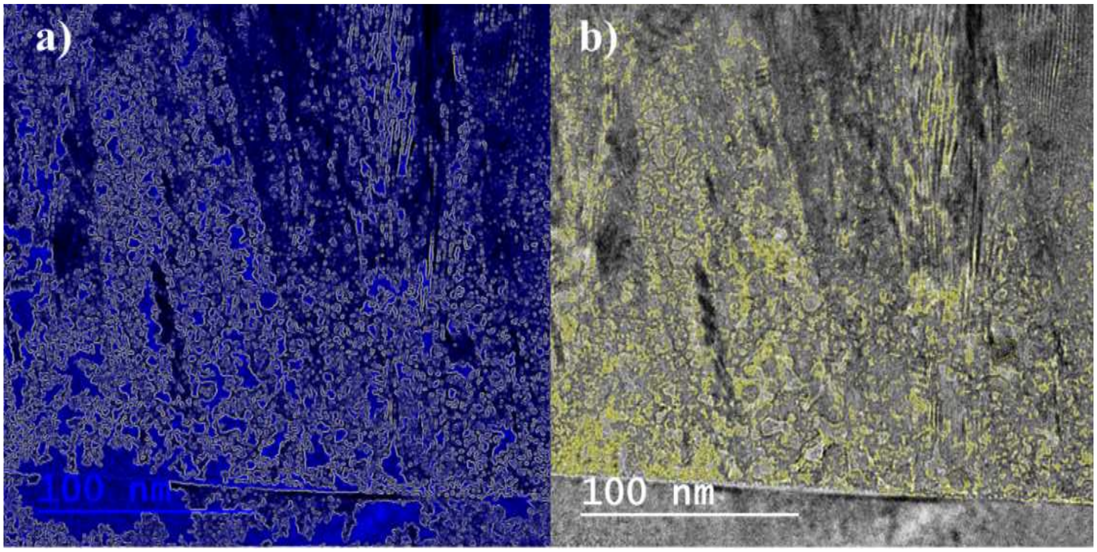

Fig. 8. a) Crystallite edge detection by a spiral phase digital filter. b) Original micrograph with overlayed 8-bit binary image (in yellow) containing simple outlines of the measured grains, which were traced by edge identification. The *analyze particles* module of the software *imagej*® was used to identify edges from the output image of the phase digital filter (a) and measure the total area of each crystallite (b).

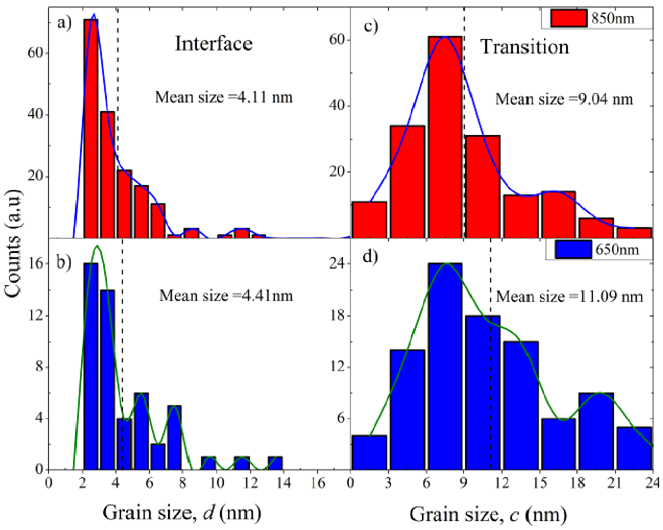

Fig. 9. Grain size distribution associated to the a), b) near interface and c), d) transition region for 640 nm and 850 nm-thick samples, respectively. The filled rectangles in the legends refer to the film thickness.

Mean sizes of 4.11 and 4.41nm were obtained in the near-interface region of 640 nm and 850 nm AlN films, respectively. Analogously, the corresponding mean size values for the transition region were 9.04 nm and 11,09 nm. The similar shapes of the grain size distributions and the proximity of the mean size values (Fig. 9) suggest that the grain size in the near-interface and the transition regions are independent of thickness. These results imply that both monolayer and multilayer AlN configurations undergo similar lattice strain relaxation and (002) grain overgrowth mechanisms.

Additionally, it was observed from statistical measurements on TEM micrographs for three different monolayer and multilayer samples that the out-of-plane alignment is completed at a film thickness of around 190 nm for all measured samples. For a larger film thickness, small grains coalesce and the aligned columnar structure develops.

The grain size distributions in the columnar region of all AlN samples were systematically studied in a similar way based on a digital SEM image processing and considering a right parallelepiped grain shape with an average length *a* for each side of the base and an average height *b* [Fig 2(b) and (c)].

It was found that the length of the columnar grains is about forty times the average columnar diameter, thus both were measured separately. The evolution of columnar diameter as a function of thickness for the AlN monolayers and multilayers is given in Fig. 10. The columnar grain diameter appears to increase with thickness. A broadening of the distribution is also observed, indicating a wider range of columnar diameters for thicker films. This fact can be explained by the competition between the nucleation rate and adatom mobility, which inhibit the coalescence of all nucleation sites. Hence, some islands do not coalesce with their neighbors, promoting the subsistence and growth of small grains.

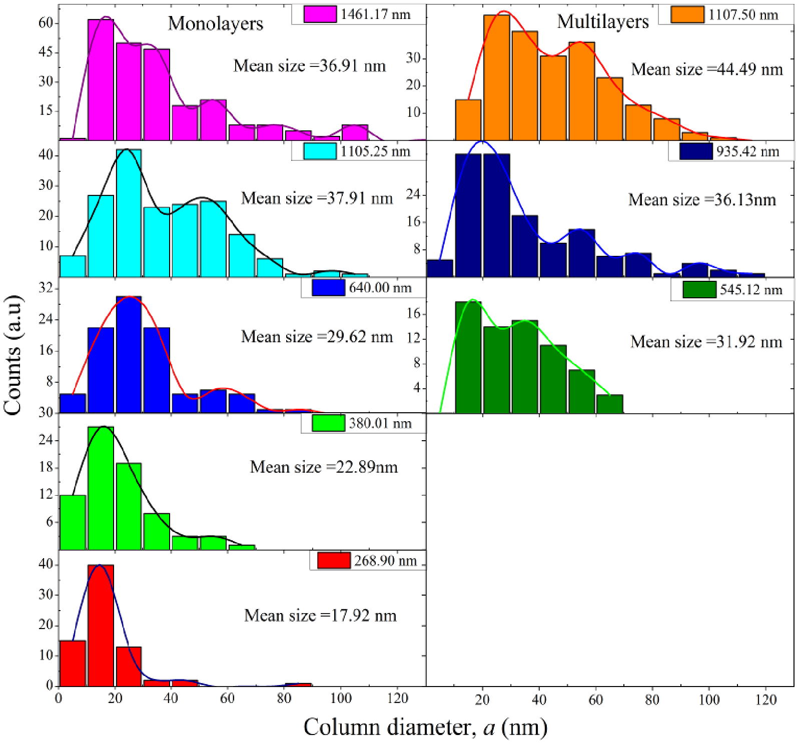

Fig. 10. Evolution of column diameter through the cross-plane of AlN a) monolayer and b) multilayer samples as a function of film thickness. The filled rectangles in the legends refer to the film thickness.

4.3 Chemical Analysis

Figure 11 shows a chemical analysis performed by energy-dispersive X-ray spectroscopy (EDX) on a 3x270 nm multilayer sample. The element distribution map shows the presence of random oxygen impurities between two successive AlN layers. Additionally, an overlap of Si and O elements at the substrate interface is observed. The continuous amorphous interlayer observed in Fig. 6(b) is a 3 nm native oxide formed at the surface of the silicon substrate. The detected homogeneous oxygen background is associated to the oxidized surface of the cooper sample holder.

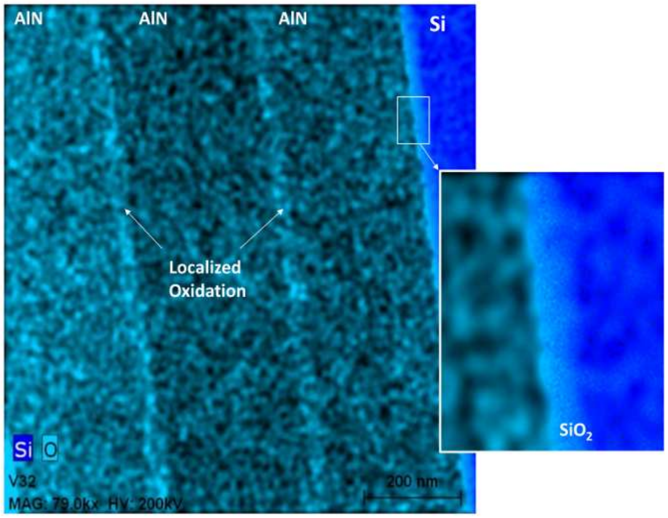

Fig. 11. Composite element distribution map performed by energy-dispersive X-ray spectroscopy (EDX) on a 3x270 nm multilayer sample. The relative distribution of silicon is presented in blue and the one of oxygen is showed in cyan. The presence of random oxygen impurities at the interface between two successive AlN layers is evidenced by the increase of oxygen concentration in the oxygen element map. The inset shows the interface between AlN and the silicon substrate. It reveals the overlap of silicon and oxygen distributions at the Si/AlN interface, which confirms the presence of a silicon dioxide interlayer formed at the silicon surface.

4.4 3-omega Thermal Conductivity Measurements

The effective thermal conductivities of the monolayer and multilayer configurations were measured by a differential 3-omega technique, assuming a one-dimensional heat conduction model to fit the real part of the experimental thermal wave amplitude as a function of the modulation frequency.

Thermal resistance as a function of the film thickness for monolayer and multilayer configurations were obtained by considering the specimens as a serial network of thermal resistances. The obtained experimental results are summarized in Table 2. The effective thermal resistances R_{eff} for the monolayer and multilayer configurations are shown in Fig. 12 as a function of the film thickness. R_{eff} includes the interfacial thermal resistances R and R_s. Assuming that R_s is equivalent for all samples, the experimental data of R_{eff} were extrapoled to $L = 0$ by using the linear model in Eq. (3) to estimate the thermal boundary resistance between the substrate and the AlN films as $R_s = 62.74 \times 10^{-9} \mathrm{m^2KW^{-1}}$, for both the monolayer and multilayer configurations. Here, R_s includes the overall resistive contributions of the near-interface and transition regions. The obtained value falls within a reasonable range and is in good agreement with other experimental data reported for polycrystalline AlN films deposited on silicon substrates[46,61]. The asymptotic behavior of the multilayer effective thermal resistance near small thickness values (Fig. 12) suggests that the thermal boundary resistance R_s between the AlN film layer and the Si substrate does not depend on the synthesis conditions or film thickness, but on the structures and defects of the near-interface and transition regions. The major contribution to the overall thermal resistance comes from R_s, indicating that planar defects in the near-interface and transition regions such as grain boundaries cause the largest number of diffusive scattering events of the energy carriers.

Table 2. Thermal properties measured experimentally for the monolayer and multilayer AlN films.

		L (nm)	k_{eff} ($\mathrm{Wm^{-1}K^{-1}}$)	R_{eff}[a] ($10^{-9}\ \mathrm{m^2KW^{-1}}$)	R[b] ($10^{-9}\ \mathrm{m^2KW^{-1}}$)
Monolayers		268.9	3.12 ± 0.26	86.16 ± 2.31	
		380.1	4.27 ± 0.17	89.01 ± 2.13	
		640.0	5.86 ± 0.27	109.29 ± 2.79	
		1105.2	7.41 ± 0.23	149.13 ± 5.22	
		1461.2	8.21 ± 0.36	178.06 ± 4.76	
Multilayers	2x270	545.1	5.07 ± 0.36	107.43 ± 2.70	12.45
	3x270	935.4	5.84 ± 0.31	160.21 ± 4.17	12.38
	4x270	1107.5	5.93 ± 0.22	186.90 ± 4.89	12.52

[a] The effective thermal resistance was calculated with Eq.(3), by considering the whole system as a serial network of thermal resistances.

[b] The thermal boundary resistance R at interfaces between two AlN layers was determined with Eq.(4).

The obtained thermal boundary resistance between the substrate and AlN films was estimated to $R_s = 62.74 \times 10^{-9} \mathrm{m^2KW^{-1}}$.

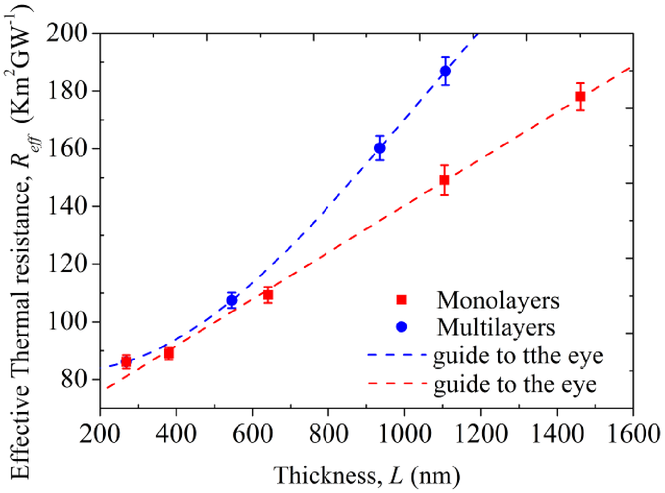

Fig. 12. Effective thermal resistance as a function of the film thickness, for the monolayer and multilayer configurations.

This result can be explained with Eq. (11), which highlights that the effect of the Kapitza resistance at the interface between grains becomes stronger for smaller grains, when the grain size is comparable or smaller than the Kapitza radius $d_n \leq a_{Kg}$. From the theoretical model, the Kapitza radius for AlN was estimated to be $a_{Kg} = 60\text{nm}$ and from statistical analysis of TEM images, experimental mean grain sizes of $d_I \approx 4\text{ nm}$ and $d_T \approx 10\text{ nm}$ were measured for the near-interface and transition regions, respectively. The corresponding phonon MFPs in these regions were estimated to be $D_I \approx 3.94\text{ nm}$ and $D_T \approx 9.32\text{ nm}$. Therefore, the dominant role of the thermal boundary resistance R_s in the thermal transport across polycrystalline films is owed to the carrier-boundary scattering mechanisms. The dominant scattering mechanisms in the near-interface and transition regions are thus mainly due to the small grain size compared to the Kapitza radius ($d_n << a_{Kg}$), to the decrease of the phonon MFPs and to the diffusive scattering at the substrate-layer interface. The obtained values of the interface thermal resistance R at the interface between two AlN layers are reported in the last column of Table 2. Despite the fact that the major contribution to the overall thermal resistance is given by R_s, the considerable values of R measured in multilayers, suggest that phonons also undergo significant diffusive scattering by oxygen related defects localized between two AlN layers. Equation (14) indicates that the contribution of R and R_s to the reduction of the effective thermal conductivity k_{eff} is determined by their corresponding values presented in Table 2 with respect to the total film thickness.

The experimental effective thermal conductivity k_{eff} as a function of the film thickness and in comparison with its theoretical predictions determined with Eq. (14) is shown in Fig. 13, for both the monolayer and multilayer configurations. The predictions of the developed model for thermal conductivity of polycrystalline films match quite well the experimental data, with an error below 10%. The slight theoretical overestimation of k_{eff} for both monolayer and multilayer can be attributed to the *regular grain geometry* approximation. As shown in Fig. 8, the near-interface and the transition regions are composed of grains with irregular shapes and different sizes, yet the modeled structure was approximated as a serial assembly of cubic grains. However, the simple theoretical model developed in section 3 yields remarkably satisfactory predictions of the thermal conductivity of the polycrystalline AlN films.

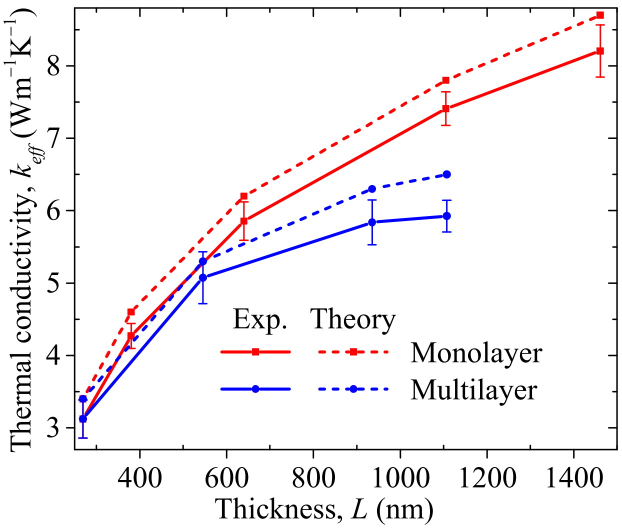

Fig. 13. Comparison between the experimental and theoretical values of the effective thermal conductivity of grained monolayers and multilayers, as a function of the film thickness.

Figure 13 shows that surface scattering of the energy carriers increases as the film thickness decreases, which reduces k_{eff}, as expected. Thickness dependence of the thermal conductivity can be interpreted by accounting for the non-homogeneity of the grain structure through the cross-plane of the films, as confirmed by the theoretical model. Structural disorder at the near-interface region, main lattice strain relaxation, and growth mechanisms cause the grain structure evolution through the c-axis. The systematic TEM study (Fig. 6, Fig. 7 and Fig. 8) confirms that crystalline structure and microstructure evolve with thickness and therefore it modifies the phonon transport properties through the cross-plane. Results in Fig. 13 indicate a significant overall reduction in thermal conductivity of multilayer films. For example, the effective thermal conductivity of a 1107.5 nm thick multilayer sample is 5.92 Wm^{-1} K^{-1}, which represents a 20% decrease when compared to that of a monolayer film of approximately equivalent thickness. The drop of the effective thermal conductivity along with the element distribution map shown in Fig. 11 indicates that the random oxygen impurities at the AlN/AlN interfaces, act as thermal barriers for phonons. Given that the thermal resistance at the interface between the substrate and the AlN film is constant and equivalent for all samples, and that the effect of the thermal resistance R associated to the interfacial oxidation increases with the number of layers, as explicitly established in Eq. 14, the reduction of the thermal conductivity of the multilayer structure with respect to its values in the monolayer one, is due to the strong impact of the oxygen impurities. It is therefore clear that the cross plane thermal conductivity of thin films with structural inhomogeneity can be effectively tailored not only by controlling the grain size at the near-interface, transition, and columnar regions, as is the case of monolayers, but also by adding localized oxidation.

5 Conclusions

The impact of local oxidation and morphology evolution of grains along the cross plane direction of polycrystalline films of Aluminum Nitride on their thermal conductivity has been investigated both experimentally and theoretically. Thickness dependent thermal conductivity measurements have been carried out by the differential 3-omega technique on monolayer and multilayer AlN samples. The diffusive scattering by oxygen-related defects localized at the interface between two AlN layers has been studied by thermal measurements of the multilayered configuration. Furthermore, the grain structure evolution has been also investigated by the statistical analysis of digitally processed micrographs obtained with electron transmission and scanning microscopy. Structural features have been correlated to the thermal properties by a simple yet accurate theoretical model, which takes into account the distribution of the grain geometry and considers the films as a serial assembly of three layers, composed of parallelepiped grains. The experimental values of the thermal conductivity of the monolayer and multilayer AlN polycrystalline films are well predicted by the developed model, with a deviation of less than 10%. The results reported in this work provide an experimental approach to perform a structural characterization of polycrystalline films, and describe their thickness-dependent thermal conductivity through an analytical model. The introduction of random oxygen impurities at the interface between AlN layers presented in this work provides a simple and inexpensive method to reduce thermal conductivity of thin films. Our theoretical and experimental results for AlN can be extended to other materials of great interest in new technological applications such as GaN, diamond, or ZnO, which usually exhibit the characteristic structural non-homogeneity.

Acknowledgements

We thank N. PELISSIER from CEA-Liten Grenoble, for her helpful assistance in preparing the TEM samples and her collaboration for the transmission electron microscopy (TEM) analysis. We acknowledge Dr. D. SIERRA from the Centro de Investigaciones Opticas (CIOp) at the Universidad Nacional de La Plata, Argentina; for kindly providing the spiral filter used to process TEM images. We thank the Laboratoire des Caractérisations Électriques from CEA-Leti for the electrical characterization facilities. We express our gratitude for financial support from CARNOT *énergies du Futur* and from the ANR-Agence Nationale pour la Recherche- project nanoTHERMA.

6 Notes and references

[a] Laboratoire de Récupération des Micro-énergies LITEN/DTNM/SERE, CEA, 38000 Grenoble, France.

[b] Laboratoire d'Énergétique Moléculaire et Macroscopique, Combustion, UPR CNRS 288, Ecole Centrale Paris, Grande Voie des Vignes, 92295 Châtenay Malabry, France.

*** Corresponding author**
Email: sebastian.volz@ecp.fr
Phone: +33 1 41 13 10 70

1. D. G. Cahill, *J. Vac. Sci. Technol. A Vacuum, Surfaces, Film.*, 1989, **7**, 1259.
2. B. E. Belkerk, M. a Soussou, M. Carette, M. a Djouadi and Y. Scudeller, *J. Phys. D. Appl. Phys.*, 2012, **45**, 295303.
3. M. Adamik, P. Barna and I. Tomov, *Thin Solid Films*, 1998, **317**, 64–68.
4. P. Barna and M. Adamik, *Thin Solid Films*, 1998, **317**, 27–33.
5. A. F. Júnior and D. Shanafield, *Cerâmica*, 2004, **50**, 247–253.
6. J. Luo, D. Billep, T. Waechtler, T. Otto, M. Toader, O. Gordan, E. Sheremet, J. Martin, M. Hietschold, D. R. T. Zahn and T. Gessner, *J. Mater. Chem. A*, 2013, **1**, 7576.
7. A. Mayadas and M. Shatzkes, *Phys. Rev. B*, 1970, **1**.
8. T. Tynell, A. Giri and J. Gaskins, *J. Mater. Chem. A*, 2014, **2**, 12150–12152.
9. C. K. Majumdar, *J. Math. Phys.*, 1969, **10**, 1388.
10. G. H. Tang, Y. Zhao, G. X. Zhai and C. Bi, *J. Appl. Phys.*, 2011, **110**, 046102.
11. J. E. Turney, a. J. H. McGaughey and C. H. Amon, *J. Appl. Phys.*, 2010, **107**, 024317.
12. J. Ordonez-Miranda and L. Tranchant, *Appl. Phys. Express*, 2014, **7**, 035201.
13. G. Chen, *Phys. Rev. B*, 1998, **57**, 958–973.
14. S. Xiong, K. Yang, Y. a. Kosevich, Y. Chalopin, R. D'Agosta, P. Cortona and S. Volz, *Phys. Rev. Lett.*, 2014, **112**, 114301.
15. K. Fuchs, *Math. Proc. Cambridge Philos. Soc.*, 1938, **34**, 100–108.
16. K. Esfarjani, G. Chen and H. T. Stokes, *Phys. Rev. B*, 2011, **84**, 085204.
17. J. Ordonez-Miranda, L. Tranchant, Y. Chalopin, T. Antoni and S. Volz, *J. Appl. Phys.*, 2014, **115**, 054311.
18. B. Latour, S. Volz and Y. Chalopin, *Phys. Rev. B*, 2014, **90**, 014307.
19. M. Kazan, G. Guisbiers, S. Pereira, M. R. Correia, P. Masri, a. Bruyant, S. Volz and P. Royer, *J. Appl. Phys.*, 2010, **107**, 083503.
20. C. Glassbrenner and G. Slack, *Phys. Rev.*, 1964, **1431**.
21. R. Yu, N. Tea, M. Salamon, D. Lorents and R. Malhotra, *Phys. Rev. Lett.*, 1992, **13**, 2050–2053.
22. M. Crommie and A. Zettl, *Phys. Rev. B*, 1990, **41**, 978–982.
23. Z. H. Z. Hao, L. Z. L. Zhichao, T. L. T. Lilin, T. Z. T. Zhimin, L. L. L. Litian and L. Z. L. Zhijian, *2006 8th Int. Conf. Solid-State Integr. Circuit Technol. Proc.*, 2006.
24. R. Yu, M. Salamon, J. Lu and W. Lee, *Phys. Rev. Lett.*, 1992, **69**, 1431–1434.
25. L. Wei, P. Kuo and R. Thomas, *Phys. Rev. Lett.*, 1993, **70**, 3764–3767.

26. L. Braginsky, N. Lukzen, V. Shklover and H. Hofmann, *Phys. Rev. B*, 2002, **66**, 134203.
27. H. Yang, G. Bai, L. Thompson and J. Eastman, *Acta Mater.*, 2002, **50**, 2309–2317.
28. Q. Hao, G. Zhu, G. Joshi, X. Wang, A. Minnich, Z. Ren and G. Chen, *Appl. Phys. Lett.*, 2010, **97**, 063109.
29. K. Miyazaki, T. Arashi, D. Makino and H. Tsukamoto, *IEEE Trans. Components Packag. Technol.*, 2006, **29**, 247–253.
30. R. Yang, G. Chen, M. Laroche and Y. Taur, *J. Heat Transfer*, 2005, 127, 298.
31. M. Kazan and S. Volz, *J. Appl. Phys.*, 2014, **115**, 073509.
32. Q. Hao, *J. Appl. Phys.*, 2012, **111**, 014307.
33. Q. Hao, *J. Appl. Phys.*, 2014, **116**, 034305.
34. Q. Hao, G. Chen and M.-S. Jeng, *J. Appl. Phys.*, 2009, **106**, 114321.
35. G. Chen and C. Dames, in *Thermoelectrics Handbook*, CRC Press, 2005, pp. 16–42.
36. M. Jeng, R. Yang, D. Song and G. Chen, *J. Heat Transfer*, 2008, **130**, 042410.
37. C.-W. Nan, *Prog. Mater. Sci.*, 1993, **37**, 1–116.
38. J.-H. Song, J.-L. Huang, J. C. Sung, S.-C. Wang, H.-H. Lu and D.-F. Lii, *Thin Solid Films*, 2011, **519**, 4212–4215.
39. M. Assouar, M. El Hakiki and O. Elmazria, *Diam. Relat. Mater.*, 2004, **13**, 1111–1115.
40. G. Knuyt, C. Quaeyhaegens, J. D'Haen and L. M. Stals, *Thin Solid Films*, 1995, **258**, 159–169.
41. M. Signore, E. Bellini and A. Taurino, *J. Phys. Chem. Solids*, 2013, **74**, 1444–1451.
42. K. A. Aissa, N. Semmar, D. D. S. Meneses, L. Le Brizoual, M. Gaillard, a Petit, P.-Y. Jouan, C. Boulmer-Leborgne and M. a Djouadi, *J. Phys. Conf. Ser.*, 2012, **395**, 012089.
43. S. R. Choi, D. Kim, S.-H. Choa, S.-H. Lee and J.-K. Kim, *Int. J. Thermophys.*, 2006, **27**, 896–905.
44. Y. Zhao, C. Zhu, S. Wang, J. Z. Tian, D. J. Yang, C. K. Chen, H. Cheng and P. Hing, *J. Appl. Phys.*, 2004, **96**, 4563.
45. T. Yagi, N. Oka, T. Okabe, N. Taketoshi, T. Baba and Y. Shigesato, *Jpn. J. Appl. Phys.*, 2011, **50**, 11RB01.
46. C. Duquenne, M.-P. Besland, P. Y. Tessier, E. Gautron, Y. Scudeller and D. Averty, *J. Phys. D. Appl. Phys.*, 2012, **45**, 015301.
47. A. Jacquot, B. Lenoir, A. Dauscher, P. Verardi, F. Craciun, M. Stölzer, M. Gartner and M. Dinescu, *Appl. Surf. Sci.*, 2002, **186**, 507–512.
48. V. Felmetsger, *J. Vac. Sci. Technol. A*, 2011, **29**, 021014.
49. G. Piazza, V. Felmetsger, P. Muralt, R. H. Olsson III and R. Ruby, *MRS Bull.*, 2012, **37**, 1051–1061.
50. D. G. Cahill, *Rev. Sci. Instrum.*, 1990, **61**, 802.
51. A. Jacquot, B. Lenoir and A. Dauscher, *J. Appl. Phys.*, 2002, **91**, 4733–4738.
52. A. N. Smith and P. M. Norris, in *Heat Transfer Handbook*, eds. A. Bejan and A. Kraus, John Wiley & Sons, Inc., 2003, pp. 1309–1357.
53. K. Saga, H. Kuniyasu and T. Hattori, *Test. Electrochem.*, 1999, **1**, 1–3.
54. J. Choi, J. Lee and J. Kim, *Thin Solid Films*, 2001, **384**, 166–172.
55. T. Borca-Tasciuc, A. R. Kumar and G. Chen, *Rev. Sci. Instrum.*, 2001, **72**, 2139.
56. A. Majumdar, *J. Heat Transfer*, 1993, **1**, 7–16.
57. G. Chen, *Nanoscale Energy Transport and Conversion*, Oxford University Press, 2005.
58. B. Hwang, *J. Phys. D. Appl. Phys.*, 2001, **34**, 2469–2474.
59. V. Darakchieva, J. Birch, M. Schubert, T. Paskova, S. Tungasmita, G. Wagner, A. Kasic and B. Monemar, *Phys. Rev. B*, 2004, **70**, 0454111–04541110.
60. B. Cullity, *Elements of X-ray diffraction*, Addison-Wesley Series in Metallurgy and Materials, 2nd editio., 1978.
61. K. Ait Aissa, a. Achour, J. Camus, L. Le Brizoual, P.-Y. Jouan and M. -a. Djouadi, *Thin Solid Films*, 2014, **550**, 264–267.
62. G. Radtke, M. Couillard, G. a. Botton, D. Zhu and C. J. Humphreys, *Appl. Phys. Lett.*, 2012, **100**, 011910.
63. A. Shetty, *Ph.D. thesis*, 2012.
64. B. E. Belkerk, A. Soussou, M. Carette, M. a. Djouadi and Y. Scudeller, *Appl. Phys. Lett.*, 2012, **101**, 151908.

Tunable Thermal Conductivity of Thin Films of Polycrystalline AlN by Structural Inhomogeneity and Interfacial Oxidation

J. Jaramillo-Fernandez [a], J. Ordonez-Miranda [b], E. Ollier [a] and S. Volz [b*]

[a] Laboratoire de Récupération des Micro-énergies LITEN/DTNM/SERE, CEA, 38000 Grenoble, France.

[b] Laboratoire d'Énergétique Moléculaire et Macroscopique, Combustion, UPR CNRS 288, Ecole Centrale Paris, Grande Voie des Vignes, 92295 Châtenay Malabry, France.

*** Corresponding author**

Email: sebastian.volz@ecp.fr

Phone: +33 1 41 13 10 70

Supplementary Material.

XRD θ–2θ scan patterns (in logarithmic scale) of the AlN films performed at a zoomed 2θ angle range, from 34° to 38°. The slight (002) peak shift towards higher angles when increasing film thickness can be clearly observed by plotting the logarithm of the relative diffracted intensity as a function of the 2θ angle, from 34° to 38°. The thickness dependent 2θ angle varies from 35.8° to 36.04° for monolayer films, with thicknesses varying from 270nm to 1460nm. The same 2θ angle shift is observed for multilayer films of thicknesses varying from 270nm to 1107nm. This slight (002) peak shift towards higher angles when increasing film thickness results from the strain relaxation mechanisms occurring through the cross-plane[1].

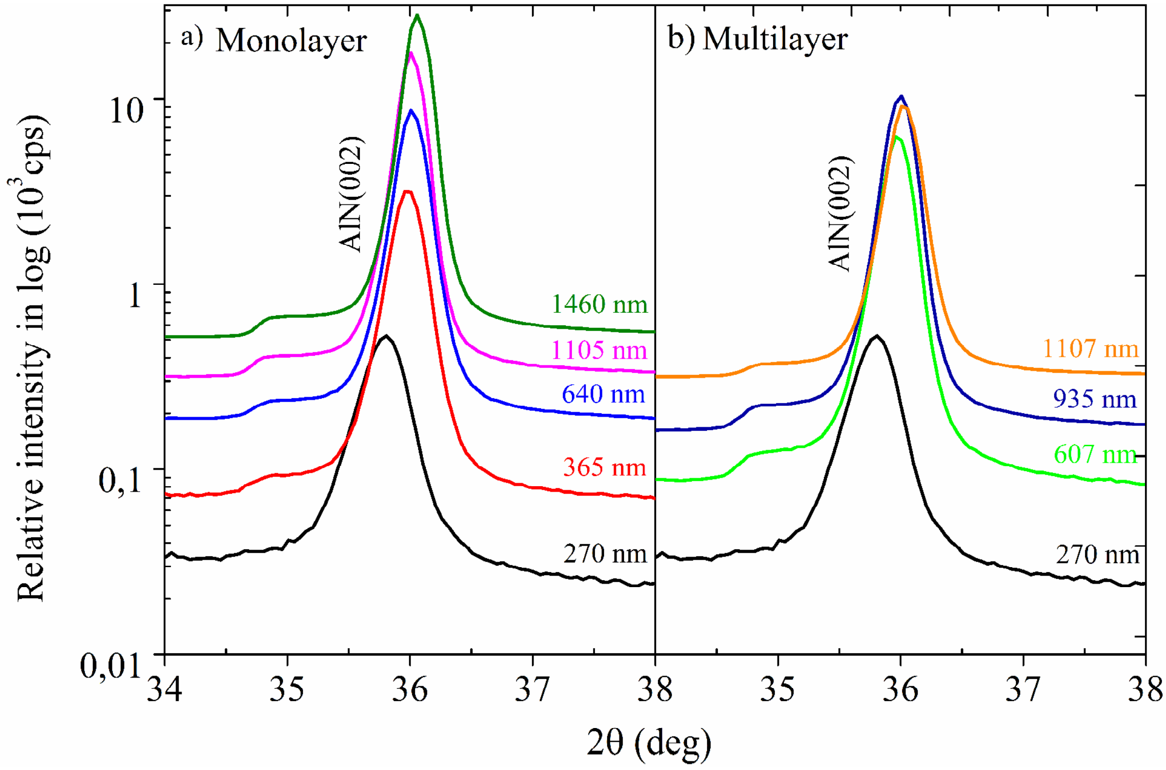

Fig. S1. XRD θ–2θ scan patterns (in logarithmic scale) of the AlN a) monolayer and b) multilayer films of different thicknesses. For both monolayer and multilayer configurations, a (002) peak shift from 2θ = 35.8° to 36.04° is observed as a result of the strain relaxation mechanisms occurring through the cross-plane[1].

TEM Fast Fourier transform pattern of Si(100)

Fig. S2 show the typical pattern of crystalline (100) Si which agree with the literature [2]. The FFT pattern obtained from a cross sectional HRTEM micrograph of the Si/AlN interface, captured with the electron beam parallel to the [0 1 1] Si zone axis.

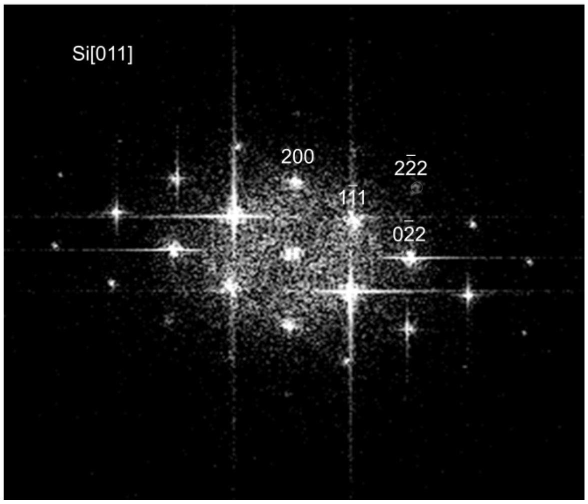

Fig. S2. Fast Fourier transform pattern from (100) single crystal silicon obtained from a cross sectional HRTEM micrograph of the Si/AlN interface, captured with the electron beam parallel to the [011] zone axis.

1 References

1. V. Darakchieva, J. Birch, M. Schubert, T. Paskova, S. Tungasmita, G. Wagner, A. Kasic and B. Monemar, *Phys. Rev. B*, 2004, **70**, 0454111–04541110.

2. A. Galca, G. Stan, L. Trinca, C. Negrila and L. Nistor, *Thin Solid Films*, 2012, **524**, 328–333.